

Projection correlation based view interpolation for cone beam CT: primary fluence restoration in scatter measurement with a moving beam stop array

To cite this article: Hao Yan *et al* 2010 *Phys. Med. Biol.* **55** 6353

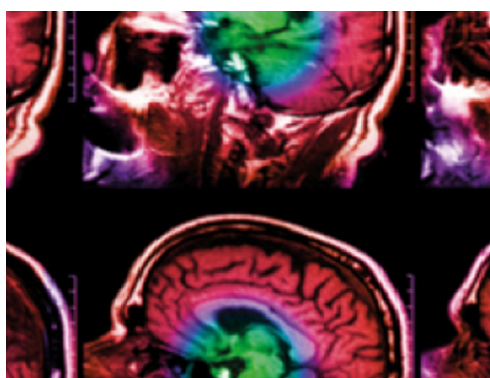
View the [article online](#) for updates and enhancements.

Related content

- [Patient-specific scatter correction for flat-panel detector-based cone-beam CT imaging](#)
Wei Zhao, Stephen Brunner, Kai Niu *et al.*
- [Experimental measurement of x-ray scatter](#)
A Akbarzadeh, M R Ay, H Ghadiri *et al.*
- [High-fidelity artifact correction for cone-beam CT imaging of the brain](#)
A Sisniega, W Zbijewski, J Xu *et al.*

Recent citations

- [Scatter Correction for Spectral CT Using a Primary Modulator Mask](#)
Odran Pivot *et al*
- [An Imperceptible Incorrectness in Deriving Data Consistency Condition from John's Equation for Cone-beam CT Imaging](#)
Shaojie Tang *et al*
- [Learningbased CBCT correction using alternating random forest based on auto context model](#)
Yang Lei *et al*



IPEM | IOP

Series in Physics and Engineering in Medicine and Biology

Your publishing choice in medical physics,
biomedical engineering and related subjects.

Start exploring the collection—download the
first chapter of every title for free.

Projection correlation based view interpolation for cone beam CT: primary fluence restoration in scatter measurement with a moving beam stop array

Hao Yan¹, Xuanqin Mou¹, Shaojie Tang¹, Qiong Xu¹ and Maria Zankl²

¹ Institute of Image Processing & Pattern Recognition, Xi'an Jiaotong University, Xi'an, Shaanxi 710049, People's Republic of China

² Helmholtz Zentrum München-German Research Center for Environmental Health, Institute of Radiation Protection, Neuherberg, Germany

E-mail: xqmou@mail.xjtu.edu.cn

Received 18 February 2010, in final form 23 August 2010

Published 12 October 2010

Online at stacks.iop.org/PMB/55/6353

Abstract

Scatter correction is an open problem in x-ray cone beam (CB) CT. The measurement of scatter intensity with a moving beam stop array (BSA) is a promising technique that offers a low patient dose and accurate scatter measurement. However, when restoring the blocked primary fluence behind the BSA, spatial interpolation cannot well restore the high-frequency part, causing streaks in the reconstructed image. To address this problem, we deduce a projection correlation (PC) to utilize the redundancy (over-determined information) in neighbouring CB views. PC indicates that the main high-frequency information is contained in neighbouring angular projections, instead of the current projection itself, which provides a guiding principle that applies to high-frequency information restoration. On this basis, we present the projection correlation based view interpolation (PC-VI) algorithm; that it outperforms the use of only spatial interpolation is validated. The PC-VI based moving BSA method is developed. In this method, PC-VI is employed instead of spatial interpolation, and new moving modes are designed, which greatly improve the performance of the moving BSA method in terms of reliability and practicability. Evaluation is made on a high-resolution voxel-based human phantom realistically including the entire procedure of scatter measurement with a moving BSA, which is simulated by analytical ray-tracing plus Monte Carlo simulation with EGSnrc. With the proposed method, we get visually artefact-free images approaching the ideal correction. Compared with the spatial interpolation based method, the relative mean square error is reduced by a factor of 6.05–15.94 for different slices. PC-VI does well in CB redundancy mining; therefore, it has further potential in CBCT studies.

1. Introduction

In kilovoltage (kV) CT imaging, flat-panel cone beam (CB) CT is an important point of focus for researchers because of the full volume coverage it offers with high isotropic spatial resolution. One major difficulty in CBCT is the serious image degradation caused by the high amount of scattered radiation at large cone angles (Siewerdsen and Jaffray 2001). Scatter-suppressing techniques include increasing air gap (Persliden and Carlsson 1997), anti-scatter grid (Floyd *et al* 1994) and the bowtie method (Graham *et al* 2007). However, these techniques can eliminate only part of the scattered radiation. Therefore, much effort is being made for scatter correction, namely removing the scatter fluence from scatter-contaminated projections. Different correction strategies are proposed, such as the scatter kernel calculation (Rinkel *et al* 2007, Maltz *et al* 2008a, Li *et al* 2008, Meyer *et al* 2010), analytical computation (Boone 1988, Spies *et al* 2000, Yao and Leszczynski 2009a, 2009b), Monte Carlo (MC) simulation (Zbijewski and Beekman 2006, Kyriakou *et al* 2006, Mainegra-Hing and Kawrakow 2008, Poludniowski *et al* 2009), primary modulation (Maltz *et al* 2005, Zhu *et al* 2006) and scatter-measurement method (Love *et al* 1987, Ning *et al* 2004, Zhu *et al* 2004, Schlattl *et al* 2006, Siewerdsen *et al* 2006, Cai *et al* 2008, Maltz *et al* 2008b, Zhu *et al* 2009a).

In scatter kernel calculations, the scatter fluence is represented as convolution of scatter kernel and primary fluence, i.e. it can be removed once the scatter kernel is estimated. By using the scatter data measured with water-equivalent tissues (WET), the kernel is estimated with pre-calculation together with online calibration (Rinkel *et al* 2007), edge spread function (ESF) calculation (Li *et al* 2008) or MC modelling (Maltz *et al* 2008a, Meyer *et al* 2010). The kernel is approximately modelled and estimated, so extra calibration or parameter tuning is necessary for a variety of scanning objects.

Analytical computation is based on the Klein–Nishina formula, which needs unknown prior information on the spectrum, object properties of geometry and attenuations; therefore, analytical methods are mostly model based (Boone 1988, Spies *et al* 2000). Yao and Leszczynski (2009a) report that the prior information can be reasonably approximated, and thus the first-order Compton scatter has functional relations with the primary fluence. This idea is also evaluated with heterogeneous mediums (Yao and Leszczynski 2009b). Nevertheless, further study is needed in the kV imaging domain, since the method does not well account for coherent scatter, which affects the primary fluence seriously at low energies.

MC simulation is effective but computationally demanding, especially in CBCT with many projections. Several MC based corrections have been proposed, using acceleration techniques such as Richardson–Lucy (RL) filtering (Colijn and Beekman 2004a), fixed forced detection (Poludniowski *et al* 2009), integration of variance reduction techniques (Mainegra-Hing and Kawrakow 2008) and hybrid simulation (Kyriakou *et al* 2006). For MC based methods, efforts continue to be focused on striking a balance between the level of accuracy and the cost of MC simulations.

The primary modulation method is impressive as a theory (Maltz *et al* 2005, Zhu *et al* 2006) and in terms of preliminary results (Zhu *et al* 2006). In this method, a part of the primary fluence is modulated to a high frequency. When it is demodulated, weighted and subtracted, the primary intensity is neutralized, while the scatter fluence remains. The proper parameter choice for optimal modulation is crucial in applications of this method to prevent contamination between the modulated and original primary fluence, which is important for accuracy in density and spatial resolution.

Scatter-measurement methods have attracted interest in both kV (Love *et al* 1987, Ning *et al* 2004, Zhu *et al* 2004, Siewerdsen *et al* 2006, Cai *et al* 2008) and MV (megavoltage) CBCT (Maltz *et al* 2008b, Zhu *et al* 2009a). In the initial version (Love *et al* 1987), scatter

Table 1. Comparison of scatter-measurement methods. (The normal scan dose is normalized to 1.)

Method	Appurtenance	Scan times	Total dose	Accuracy	
				Primary	Scatter
I-BSA	Static BSA	2	1.892	Excellent	Excellent
SV-BSA		2	1.044	Good	Good
SPECS	Collimator	1	1	Good	Good
Moving BSA	Moving BSA	1	0.892	Medium	Excellent

intensity is sample-measured with a beam stop array (BSA) in a view-by-view extra scan that is in addition to the normal scan. Then the scatter fluence is estimated with 2D spatial interpolation based on the measurements. When it is subtracted from the projections acquired in the normal scan, scatter correction is accomplished. The method of Love *et al* (1987) is reliable, and it has often been used as the ideal correction method in related studies (Rinkel *et al* 2007, Zhu *et al* 2009a, 2009b); this method has later been referred to as I-BSA (ideal BSA correction). However, the disadvantage of I-BSA is the approximately double dose due to the extra scan. Ning *et al* (2004) reduced the dose significantly by performing the extra scan in a sparse-view way; scatter fluence in additional views is estimated by angular interpolation based on sparse-view measurements. The version of Ning *et al* (2004) is considered to be an improvement over I-BSA because of its dose practicability. It has been later referred to as SV-BSA (sparse view BSA method).

Since extra scans cause both extra dose and operational inconvenience, methods integrating the scatter measurement into the normal scan have been proposed; e.g. the SPECS (scatter and primary estimation from collimator shadows) method (Siewerdsen *et al* 2006) in which the standard equipment (collimator) has a function similar to the BSA. The SPECS method is simple to implement. However, the measurement in the collimator shade is not always adequate for scatter fluence estimation; therefore, parameter tuning has to be performed task-dependently to prevent overcorrection (Siewerdsen *et al* 2006).

Besides SPECS, the moving BSA method (Zhu *et al* 2004) also needs only a single scan to accomplish scatter correction along with the reconstruction. With a moving BSA, scatter intensity is measured well in each view. At the same time, the primary fluence is well estimated except for the part that is in the BSA shade. In terms of the restoration of the shaded primary fluence, spatial interpolation is not adequate, although it yields good performance in scatter fluence estimates because spatial interpolation performs well predominantly in a low-frequency domain, while part of the primary fluence is not in that (low-frequency) domain. Consequently, although a raster-moving BSA is designed to prevent the primary beams from being blocked at fixed positions, thereby reducing the cumulative error, streak artefacts are typically observed in reconstructed images. This limitation is illustrated in subsequent sections.

Scatter-measurement methods are compared (table 1) with the settings in Ning *et al* (2004), where the BSA blocks 10.8% of the primary radiation and sparse views occupy 4.88% of the total views. In I-BSA and SV-BSA, the normal scan dose is normalized to 1. Hence the dose for the extra scan is 89.2% (view-by-view) and $4.88\% \times 89.2\%$ (sparse view). The dose for the moving BSA method is 10.8% less than that for the SPECS method, since the BSA blocks 10.8% of primary radiation. From table 1, we can see that the moving BSA method would be a promising method if enhanced accuracy could be achieved in primary fluence restoration, since it has high dose efficiency, and a low dose is generally a parameter of high priority.

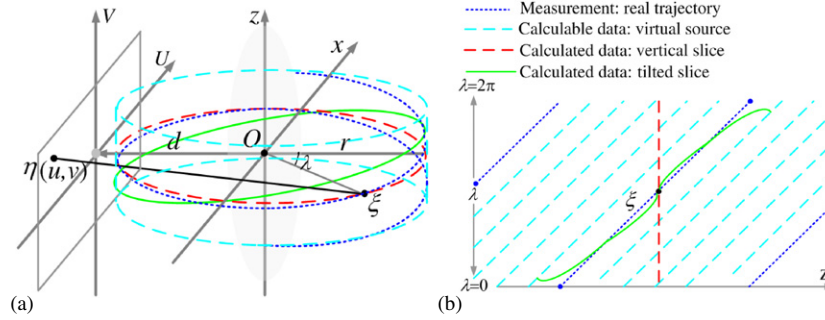


Figure 1. (a) Flat panel CBCT configuration. (b) Illustration of the seminal work in section 2.2: virtual data away from the scanning trajectory can be calculated from the measured data.

In this paper we focus on a better primary fluence restoration in the moving BSA method by considering the angular correlations among CB views. This idea had first been presented by us in the Fully3D 2009 conference (Yan *et al* 2009). In this paper, we achieve our aim by deducing a projection correlation (PC) from redundant CB views based on John's equation (John 1938, Patch 2002) (section 2). With this correlation, we develop a view interpolation method called projection correlation based view interpolation (PC-VI). The physical meaning of PC-VI is interpreted and validation is made with both noise-free and noisy projections of the FORBILD head phantom. On this basis, the working requirement of PC-VI is obtained (section 3). The proposed PC-VI is adopted for restoring the lost primary fluence in the moving BSA method. Furthermore, novel moving modes with better mechanical feasibility are suggested, instead of the original raster-moving mode. We conduct analytical (Tang *et al* 2008) and MC simulations (EGSnrc toolkit, Kawrakow and Rogers 2003) of the entire scatter-measurement procedure on an elaborate high-resolution human phantom (Petoussi-Henss *et al* 2002, Zankl *et al* 2002) to assess the performance of the PC-VI based moving BSA method by comparing it with the existing BSA based methods (section 4). The proposed methods are discussed in section 5 and conclusions are drawn in the last section.

2. Projection correlation in CB views

2.1. Preliminary: John's equation and CBCT configuration

In the CB configuration, denoting the x-ray focal spot as ξ and the detector cell as η , the weighted x-ray transform $g(\xi; \eta)$ of an object f is as follows:

$$g(\xi; \eta) = \int_{\mathbb{R}} f(\xi + t(\eta - \xi)) dt = X(f(\xi; \eta))/|\xi - \eta|. \quad (1)$$

In (1), $X(f(\xi; \eta))$ are the CT data, the normalized line integral of f . Denoting g_{xy} as the partial differential of g to the variables x and y , John's equation (John 1938) is

$$g_{\eta_i \xi_j}(\xi; \eta) - g_{\eta_j \xi_i}(\xi; \eta) = 0, \quad i, j = 1, 2, 3. \quad (2)$$

In the following text, deductions are based on flat panel CBCT configurations shown in figure 1(a), in which u and v are the 2D detector coordinates. λ is the azimuth angle. r and d are the source-to-centre and centre-to-detector distances, respectively. z is the longitudinal coordinate. View and projection are both used to refer to the weighted CT data, i.e. $g(\xi; \eta)$.

2.2. Seminal work: calculation of unmeasured data

According to the flat panel CBCT configuration, in which $g(\lambda, u, v)$ will be simply denoted as g or $g(\lambda)$ later, Patch (2002) performs a variable substitution in (2) and gets

$$g_{v\lambda} - rg_{uz} = -\frac{2u}{r+d}g_v - \frac{uv}{r+d}g_{vv} - \left(r+d + \frac{u^2}{r+d}\right)g_{uv}. \quad (3)$$

The superscript $*$ is used to represent the Fourier transform, e.g. the Fourier transform of $g(\lambda, u, v)$ is denoted as $g^*(\lambda, k_1, k_2)$, and simplified as g^* . Taking the Fourier transform to u, v in (3) results in

$$k_2g_\lambda^* - rk_1g_z^* = \frac{jk_2}{r+d} (2g_{k_1}^* + k_2g_{k_1k_2}^* - (r+d)^2k_1g^* + k_1g_{k_1k_1}^*). \quad (4)$$

Since (4) is a first-order partial differential equation (PDE) for z and λ , it can be used to calculate the unmeasured view of a virtual source with boundary conditions of the measured data (Patch 2002). As illustrated in figure 1(b), the views of virtual sources (cyan dashed line) can be calculated by the measured views of the actual trajectory (blue dotted line). However, since this calculation corresponds to extrapolation rather than interpolation, higher accuracy and practicability are more likely to be achieved for a close-distance virtual source, e.g. in Defrise *et al* (2003), data for a virtual tilted slice (green line) are calculated to improve the image reconstruction.

2.3. Our work: projection correlation between neighbouring CB views

On the basis of (3), an approximation according to the CBCT configuration is adopted first to replace z with v without losing much accuracy:

$$g_{uz} \cong g_{uv} \cdot ((r+d)^2 + u^2 + v^2)/(r(r+d)). \quad (5)$$

A similar characteristic of (5) in two dimensions is firstly used in Defrise *et al* (2003). And we get

$$g_{v\lambda} \cong -\frac{2u}{r+d}g_v - \frac{uv}{r+d}g_{vv} + \frac{v^2}{r+d}g_{uv}. \quad (6)$$

Writing it in terms of g_v ,

$$(g_v)_\lambda \cong -\frac{2u}{r+d}g_v - \frac{uv}{r+d}(g_v)_v + \frac{v^2}{r+d}(g_v)_u. \quad (7)$$

Denoting the right-hand side of (7) as $G(\lambda, g_v(\lambda))$, and if $d\lambda$ is a tiny rotation in λ , we get

$$\frac{g_v(\lambda + d\lambda) - g_v(\lambda)}{d\lambda} \cong G(\lambda, g_v(\lambda)).$$

That is,

$$g_v(\lambda + d\lambda) \cong g_v(\lambda) + d\lambda \cdot G(\lambda, g_v(\lambda)). \quad (8)$$

From (8), we can get $g_v(\lambda + d\lambda)$ from its neighbouring view $g(\lambda)$. To get $g(\lambda + d\lambda)$ itself, we make further deduction in the frequency domain, where the counterpart of (6) is

$$k_2g_\lambda^* \cong \frac{j}{r+d} (-2k_1g_{k_2}^* + k_2^2g_{k_1k_2}^* - k_1k_2g_{k_2k_2}^*). \quad (9)$$

Hence

$$g_\lambda^* \cong \frac{j}{r+d} \cdot \left(-2\frac{k_1}{k_2}g_{k_1}^* + k_2g_{k_1k_2}^* - k_1g_{k_2k_2}^*\right), \quad k_2 \neq 0. \quad (10)$$

Also denoting the right-hand side of (10) as $G(\lambda, g^*(\lambda))$, (10) could be simply written as

$$g^*(\lambda + d\lambda) \cong g^*(\lambda) + d\lambda \cdot G(\lambda, g^*(\lambda)), \quad k_2 \neq 0. \quad (11)$$

Equations (8) and (11) are the PC between neighbouring CB views. Although (8) and (11) are theoretically equivalent, they have different efficiencies in numerical implementation, which is discussed later. In this paper, all our work is based on (11). It reminds us that redundancy information is angularly contained; e.g. in the frequency domain, most frequency components of $g(\lambda + d\lambda)$ can be calculated from its neighbouring view $g(\lambda)$, except the trans-axial zero frequency $k_2 = 0$ ($k_2 \approx 0$ in practice, see section 3.2), which is in a low-frequency domain and can be estimated by spatial interpolation. Based on this thought, we develop PC-VI.

3. Projection correlation based view interpolation

3.1. Physical interpretation

An intuitive process of PC-VI is described as follows. Assume that the neighbouring projection $g(\lambda)$ and $g(\lambda + 2d\lambda)$ are complete, and our task is to restore the lost data in the view $g(\lambda + d\lambda)$. Considering that (11) holds for $k_2 \neq 0$, we use spatial interpolation as a complementary for the frequency component at $k_2 = 0$. Firstly $g(\lambda + d\lambda)$ is initially restored by the commonly used spatial interpolation, and the result is denoted as $g^{\text{IR}}(\lambda + d\lambda)$, wherein the superscript IR means *initial restoration*. This step mainly recovers the low-frequency components in lost data. Then work is carried out in the frequency domain by a PC with (11). The other frequencies (especially a high frequency) of lost data are restored in the form of $g^*(\lambda + d\lambda)$ from $g^*(\lambda)$; for $k_2 = 0$, we adopt $g^{\text{IR}*}(\lambda + d\lambda)$ directly. The neighbouring view $g(\lambda + 2d\lambda)$ can be used similarly, and combined with the result from $g(\lambda)$ with the weight w , we get $g^{\text{RR}*}(\lambda + d\lambda)$:

$$g^{\text{RR}*}(\lambda + d\lambda) = \begin{cases} w(g^*(\lambda) + d\lambda \cdot G(\lambda, g^*(\lambda))) + (1 - w)(g^*(\lambda + 2d\lambda) \\ \quad - d\lambda \cdot G(\lambda, g^*(\lambda + 2d\lambda))), & k_2 \neq 0 \\ g^{\text{IR}*}(\lambda + d\lambda), & k_2 = 0. \end{cases} \quad (12)$$

The superscript RR means refined restoration, that is, information in most frequency domains is covered by PC-VI in contrast to g^{IR} , in which only a low frequency is covered by spatial interpolation. Finally, through the inverse Fourier transform (F^{-1}), we get $g^{\text{RR}}(\lambda + d\lambda)$, as below:

$$g^{\text{RR}}(\lambda + d\lambda) = F^{-1}(g^{\text{RR}*}(\lambda + d\lambda)). \quad (13)$$

Figure 2(a) illustrates that PC-VI complements the incomplete view (cyan square dot) by using the complete measurements (blue round dot). Note that all views involved in PC-VI are from the actual trajectory. As seen in figure 2(a), it is clear that PC-VI is an interpolation to restore unmeasured data in the central view by using measurements in the neighbouring (to the left and right) views. This is quite different from the approach of Patch (2002), which is essentially an extrapolation since the computed data are from a virtual source outside the actual measured trajectory.

In the following, $g(\lambda + d\lambda)$ represents the entire projection; and $g(\lambda + d\lambda, u, v)$ represents the value at the pixel $(\lambda + d\lambda, u, v)$, whose spatially nearby pixels are defined as the adjacent pixels in the same view, e.g. $(\lambda + d\lambda, u \pm du, v \pm dv)$. When $g(\lambda + d\lambda, u, v)$ is lost, a spatial domain sketch of PC-VI (figure 2(b)) shows that firstly the initial restoration is performed with values of spatially nearby pixels (red round dots) by spatial interpolation, which well estimates the low-frequency information. Then, the result is refined by the PC using angularly nearby information (cyan area), which represents high-frequency variations from the current view

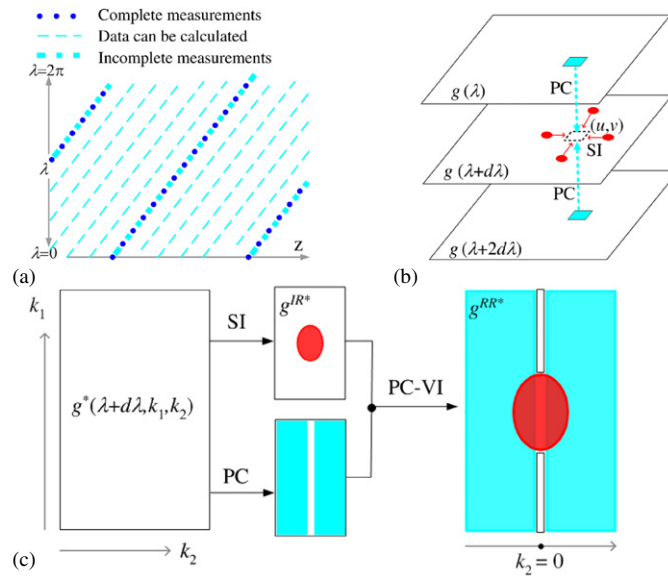


Figure 2. Physical interpretation of PC-VI. Spatial interpolation is abbreviated as SI in the figures for brevity. (a) PC-VI: incomplete views can be interpolated from complete views. (b) Spatial domain sketch of PC-VI when $g(\lambda + d\lambda, u, v)$ (in the black dotted area) is lost. Spatially nearby pixels are represented by the red dots, and angularly nearby information is contained in the cyan area. (c) The corresponding frequency domain sketch. PC-VI restoration consists of two parts: the red-circled area is contributed by spatially nearby pixels; the cyan area is contributed by angularly nearby information. The white area with a thin black frame represents the small blind zone beyond the capacity of PC-VI.

to the next view. Finally, the results of spatial interpolation and PC are combined together, and we get the PC-VI restoration. The corresponding frequency domain sketch is shown in figure 2(c) where $g^*(\lambda + d\lambda, k_1, k_2)$ represents the Fourier transform of $g(\lambda + d\lambda, u, v)$; the white area represents null information; the red-circled area represents the low-frequency information restored by spatial interpolation; and the cyan area represents the calculable frequency domain by the PC. As illustrated, spatial interpolation is a supplementary to $k_2 = 0$ for the PC, and most frequencies are recovered finally, except for the small white area framed by a thin black line.

3.2. Implementation

Given complete $g(\lambda)$, $g(\lambda + 2d\lambda)$ and incomplete $g(\lambda + d\lambda)$ with the blind pixel $(\lambda + d\lambda, u, v)$, the flow of PC-VI is as follows.

- (1) $g(\lambda + d\lambda, u, v)$ is initially restored by spatial interpolation from its spatially nearby pixels to get $g^{IR}(\lambda + d\lambda, u, v)$. Through this step, we get $g^{IR}(\lambda + d\lambda)$.
- (2) $g^{IR}(\lambda + d\lambda)$, $g(\lambda)$ and $g(\lambda + 2d\lambda)$ are transformed into the frequency domain; substituting $g^{IR*}(\lambda + d\lambda)$, $g^*(\lambda)$ and $g^*(\lambda + 2d\lambda)$ into the right-hand side of (12) with w being equal to 0.5, we get the refined restoration $g^{RR*}(\lambda + d\lambda)$.
- (3) Get $g^{RR}(\lambda + d\lambda)$ using (13). $g^{IR}(\lambda + d\lambda, u, v)$ is replaced by $g^{RR}(\lambda + d\lambda, u, v)$ and we get the first cycle of restoration, denoted as $g^{(1)}(\lambda + d\lambda)$. Note that only $g^{(1)}(\lambda + d\lambda, u, v)$ is refreshed by the calculated value, since other pixels are exactly known.

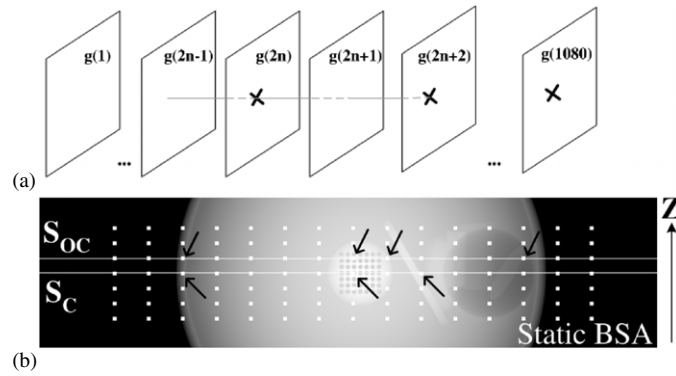


Figure 3. (a) Simulation configuration. (b) One even view blocked due to a static BSA; comparison between SI and PC-VI (first cycle) will be made by profiles along the central slice S_C and the off-centre slice S_{OC} .

- (4) Steps (1)–(3) can be performed iteratively to get further restoration $g^{(2)}(\lambda + d\lambda)$, $g^{(3)}(\lambda + d\lambda)$, etc.

In practice, we use a simple small threshold T to handle $k_2 = 0$ in step (2), namely we use a lower equation of (12) for $k_2 \leq T$ and an upper equation for $k_2 > T$. In practical implementation, the performance is not sensitive to the choice of T . The basic principle in choosing the value of T is as follows: a higher weight is given to spatial interpolation by choosing larger T in the first cycle; in subsequent cycles, a higher weight is given to the PC with decreased T . In the three cycles of the iteration, we use $T = 3, 2$ and 1 . This setting balances the weight of spatial interpolation and PC; therefore, compared with the spatial form of the PC (8), the frequency form (11) is more efficient in fully and reasonably utilizing the low-frequency information.

3.3. Validation

3.3.1. Simulation configuration. We validate PC-VI with an analytical simulation of circular CBCT projections of the FORBILD phantom³, a complex head phantom with rich high-frequency details. 1080 views of the size 850×200 are collected over 360° . The FDK algorithm (Feldkamp *et al* 1984) is used for reconstruction. Data are blocked by a static BSA with 15×7 blockers; each blocker shades 5×5 pixels. The 1080 views are alternately blocked, i.e. the even views are blocked and their neighbouring odd views are complete, as shown in figure 3(a). One blocked view is shown in figure 3(b). Validations are made on both noise-free and noisy projections (Poisson noise is added according to 750 000 photons per ray). The task is to restore the lost information using spatial interpolation as well as PC-VI, and then to make comparisons. After testing several commonly used spatial interpolation methods, we select the horizontal 1D cubic spline interpolation. This is also in accordance with the fact that the horizontal 1D interpolation introduces fewer artefacts because of the horizontal shift-invariant weighting in the FDK algorithm (Zhu *et al* 2004). Two representative slices with blind pixels, i.e. the central slice S_C and the off-centre slice S_{OC} which is 20 mm away from S_C , are investigated in terms of the average difference by reference to the complete projections.

³ Lauritsch Günter and Bruder Herbert head phantom. See <http://www.imp.uni-erlangen.de/forbild/deutsch/results/head.html>.

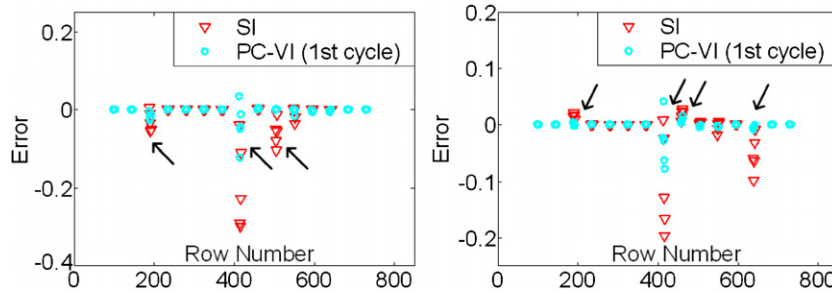


Figure 4. Comparison between SI and PC-VI (first cycle) by profiles alone S_C and S_{OC} .

Recall (7) and (8), where $d\lambda$ is supposed to be a small value. To evaluate the performance of PC-VI with various $d\lambda$, additional simulations are performed, where each view, e.g., $g(\lambda)$ is blocked and restored by PC-VI with $g(\lambda \pm d\lambda)$ one after another, where $d\lambda = i \cdot 2\pi/1080$ and $i = 1-6$. This setup corresponds to applying PC-VI with total numbers of views 1080, 540, 360, 270, 216 and 180. For each view, the absolute error is calculated by reference to the ideal projection $View_0$, as follows:

$$|Error|_{method}(\lambda) = \frac{\sum_{u,v \in B} |View_{method}(\lambda, u, v) - View_0(\lambda, u, v)|}{\sum_{u,v \in B} |View_0(\lambda, u, v)|}, \quad (14)$$

where the subscript method refers to SI or PC-VI; B represents the set of the blocked detectors.

3.3.2. Results. Figure 4 shows that with one cycle of PC-VI, significant error reduction has been achieved, especially at positions around high contrast contents as indicated by the black arrows in figure 3(b). In the reconstructed images (figure 5), the streaks due to inaccurate spatial interpolation (second column) are greatly reduced with PC-VI; a visually satisfactory restoration is achieved after three iterations. That means much more extra information could be recovered by PC-VI than by spatial interpolation. The robustness of PC-VI is also validated by the noisy images, as seen in figure 6.

The results for various $d\lambda$ are displayed in figures 7 and 8. Generally, PC-VI yields better performance in the case of denser view intervals. Compared with spatial interpolation, the enhancement by using PC-VI is significant when the total number of views declines from 1080 to 360, and it turns less significant when the views are sparsely collected, i.e. 270, 216 and 180 cases. For views losing large high-frequency contents, PC-VI always outperforms spatial interpolation even for sparsely collected views. For views losing basically low-frequency contents, PC-VI performs better for 1080 and 540 views, similar to spatial interpolation for 360 views, and it is slightly less than spatial interpolation in the case of 270, 216 and 180 views.

3.4. PC-VI requirement

In the above sections, the neighbouring views of $g(\lambda + d\lambda)$, i.e. $g(\lambda)$ and $g(\lambda + 2d\lambda)$, are assumed to be complete. In this section, we will study how PC-VI works when this assumption does not hold. We note that John's equation works locally around the source ξ and the pixel η on the detector; here *around* means the partial differential of ξ and η . In (2), we find that if $\tilde{\eta}$ (η and its neighbourhood) are unknown, partial differential to η cannot be calculated and John's equation can no longer supply redundant information. Therefore, when using John's equation, redundancy is supposed to be contained in angularly nearby pixels between adjacent

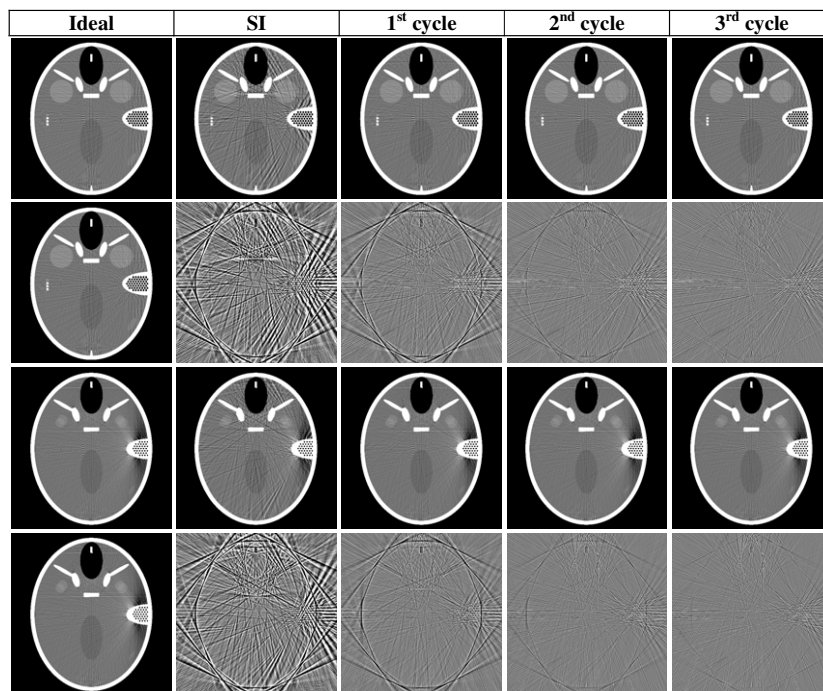


Figure 5. PC-VI performance with noise-free projections. The reconstructed images of S_C and S_{OC} are displayed in the first and third rows; the sequence from left to right is image reconstructed with complete projection, SI processed projection and projections through the first, second and third cycles of PC-VI. The displayed window is $[0, 100]$ HU. Accordingly, difference images are shown in the second and fourth rows, with a window of $[-10, 10]$ HU. In the first column of the second and fourth rows, results of third PC-VI iteration are repeated for better comparison.

views, where the angularly nearby pixel is defined as the pixel (along with its neighbourhood) with the same coordinates in adjacent views, e.g. $(\lambda, \tilde{u}, \tilde{v})$ and $(\lambda + 2d\lambda, \tilde{u}, \tilde{v})$ are the angularly nearby pixels of $(\lambda + d\lambda, u, v)$. Note that \tilde{u} represents u and its neighbourhood. We investigate (8) and find that the above analysis also holds for PC, which is reasonable since PC is derived based on John's equation. Then we get PC-VI requirement as follows.

PC-VI requirement: PC-VI works when angularly nearby pixels are complete, e.g. the calculation of $g(\lambda + d\lambda, u, v)$ needs the knowledge of $g(\lambda, \tilde{u}, \tilde{v})$ or $g(\lambda + 2d\lambda, \tilde{u}, \tilde{v})$.

In the context of the BSA blocking, we validate the PC-VI requirement with a modified simulation configuration (figure 9(a)) based on that in section 3.3.1. In this configuration, none of the 1080 views is complete due to the BSA blocking. Particularly in even views, the BSA is located fixedly at the same position and in odd views, it moves to another position, as shown in figure 9(a). We conduct eight tests. In these tests, movements of BSA shade locations between even and odd views are 0–7 pixels wide. When the movement is 0, the BSA shade is at the same location in each pair of adjacent views, so the PC-VI requirement is not satisfied. When the movement is 6–7 pixels wide, the BSA shade shifts by 6–7 pixels in each pair of adjacent views, so the PC-VI requirement is satisfied considering that the BSA shades are 5×5 pixels. Similarly, a movement of 1–5 pixels means that the PC-VI requirement is partly satisfied. We use the first cycle of PC-VI in the projection domain to illustrate its performance under the eight movements. The relative error is defined as the ratio of the refined restoration (first cycle, PC-VI) difference to the initial restoration (spatial interpolation) difference, as

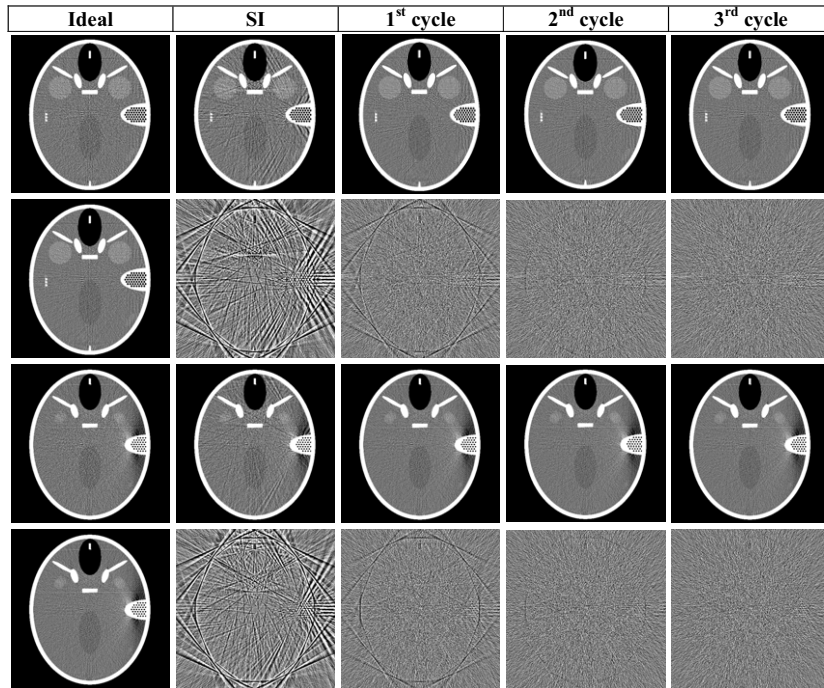


Figure 6. PC-VI performance using noisy projections. All other settings are the same as in figure 5.

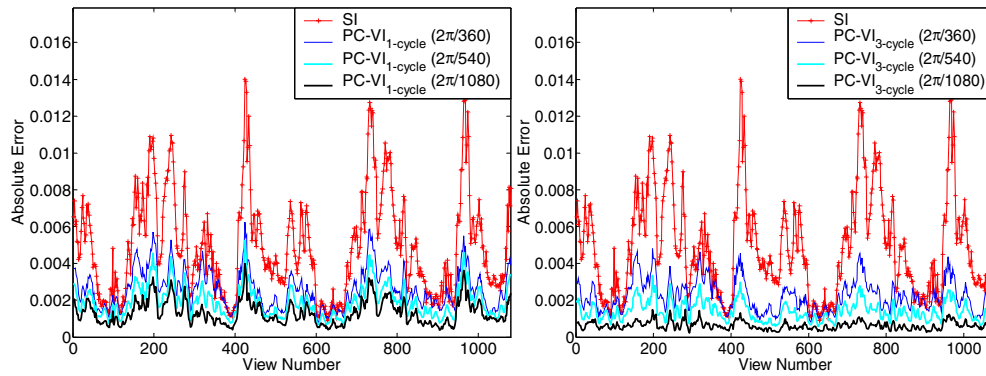


Figure 7. The performance of PC-VI under normal view intervals with (a) first and (b) third cycles of iteration. The corresponding total numbers of views are 1080, 540 and 360.

seen in (15), wherein $View_0$ represents the ideal projection. The averaged relative error is defined as a mean relative error, see (16):

$$Error_{Relative}(\lambda) = \frac{\sum_{u,v} |View_{PC-VI}(\lambda, u, v) - View_0(\lambda, u, v)|}{\sum_{u,v} |View_{SI}(\lambda, u, v) - View_0(\lambda, u, v)|}, \quad (15)$$

$$\overline{Error_{Relative}} = \frac{1}{ViewNumber} \sum_{\lambda} Error_{Relative}(\lambda). \quad (16)$$

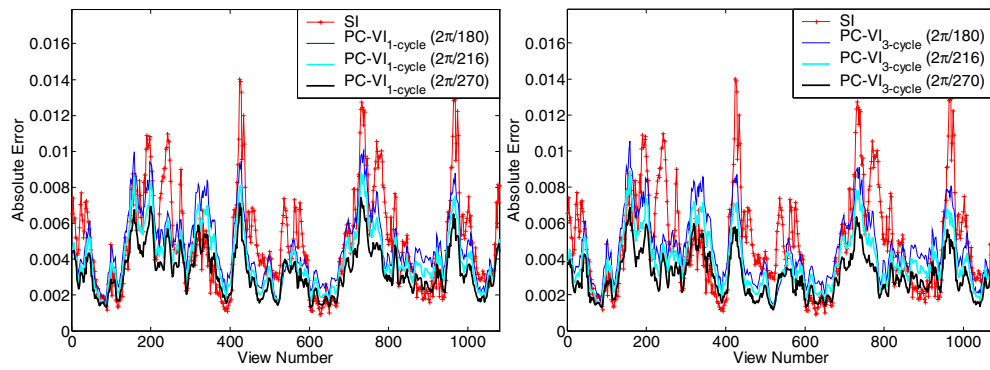


Figure 8. The performance of PC-VI under sparse view intervals with (a) first and (b) third cycles of iteration. The corresponding total numbers of views are 270, 216 and 180.

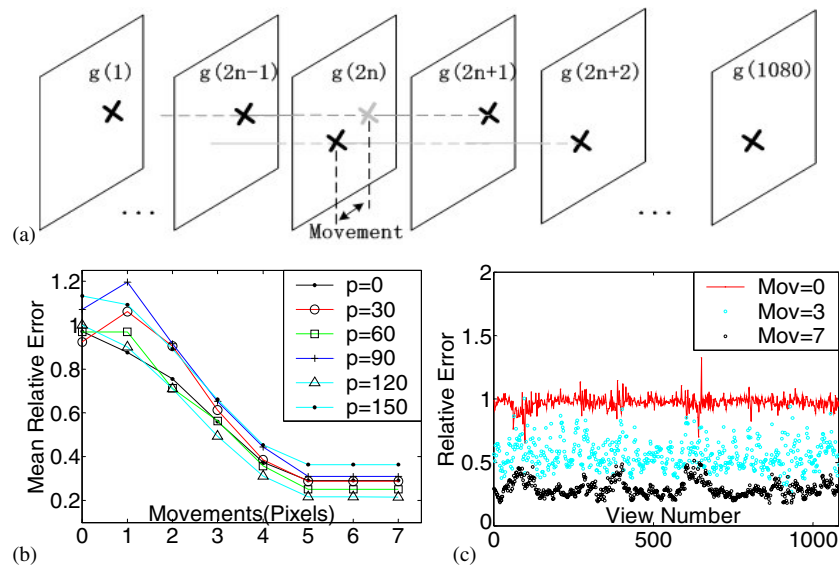


Figure 9. The performance of PC-VI under different fulfilments of the PV-VI requirement. Initial restoration errors are normalized to 1. (a) Simulation configuration, (b) mean relative error under various p (pitch (mm)) in the spiral CB scan and (c) relative error according to each view for $p = 0$. Three movements are displayed for better visibility.

The PC-VI requirement is first investigated in spiral CBCT with various pitches according to (16), and the results are shown in figure 9(b). When pitch equals zero, the relative errors according to (15) under three movements are plotted in figure 9(c). It demonstrates that when the movement is 0, PC-VI achieves little improvement compared with spatial interpolation. The accuracy of PC-VI is more evident under larger movements. When the movement is 5–7 pixels, PC-VI achieves its expected effect, totally outperforming spatial interpolation. As shown in figure 9(c), when the movement is 7 pixels wide, the relative error is far below 1 in each view, which means that the power of PC-VI is fully exhibited when the movement is larger than the blocked size.

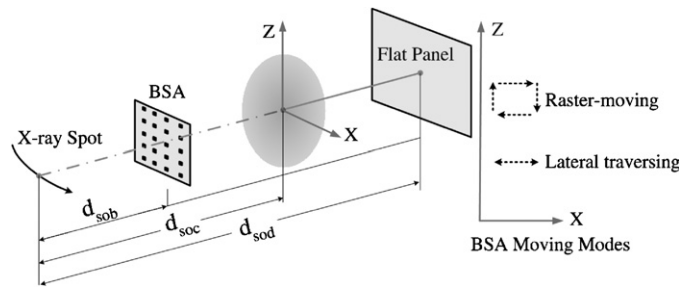


Figure 10. Scatter correction with a moving BSA setup.

In summary, PC-VI performs well when the PC-VI requirement is satisfied. To restore $g(\lambda + d\lambda, u, v)$, the PC-VI requirement only needs the complete values of the angularly nearby pixels, i.e. $g(\lambda, \tilde{u}, \tilde{v})$ and $g(\lambda + 2d\lambda, \tilde{u}, \tilde{v})$, instead of the full complete views $g(\lambda)$ and $g(\lambda + 2d\lambda)$. Therefore, this requirement is easy to be satisfied when the BSA movement is larger than the size of the single blocker shade. On the other hand, PC-VI is less effective when the PC-VI requirement is fulfilled to a lesser degree. When both $g(\lambda, \tilde{u}, \tilde{v})$ and $g(\lambda + 2d\lambda, \tilde{u}, \tilde{v})$ are lost, the accuracy of PC-VI will be degraded to a level similar to spatial interpolation. For this reason, in the context of (the next section) accomplishing both BSA measurement and reconstruction with a single scan, the lost information cannot be restored if a static BSA is used, since the PC-VI requirement is not satisfied totally. This is the reason why we need the BSA moving rather than being static.

4. PC-VI based scatter correction with a moving BSA

4.1. Seminal work: raster-moving BSA method

In the raster-moving BSA method (Zhu *et al* 2004), firstly, one scan with the raster-moving BSA is performed (figure 10), and in each view, the scatter fluence is estimated and removed using the measurements obtained with the moving BSA. After this step, scatter-free projections are acquired. Next, the blocked primary fluence is restored by the horizontal 1D cubic spline interpolation; this completes the whole correction process. In the reconstructed image, streak artefacts are reduced to some certain extent by the lower cumulated error made possible by the design of the raster-moving mode.

There are two problems in primary fluence restoration attributable to the limitation of spatial interpolation. Firstly, the blocker size has to be as small as possible, which leads to difficulty in manufacturing the BSA. Secondly, artefacts are still visible around the high-frequency contents, especially in edges between bone and air or muscles. Particularly, in the reconstructed volume, some slices are always in the shade when the raster-moving BSA is moving in the lateral direction, so the cumulated error in these slices is reduced only to a limited extent and serious artefacts remain, which is exhibited in section 4.3.

4.2. PC-VI based improved moving BSA method

The essential improvement in our method is achieved by replacing spatial interpolation with PC-VI for the primary fluence restoration. When the BSA is moving from one view to the next, the PC-VI requirement is easy to be fulfilled by simply ensuring that the BSA movement

is larger than the width of the shaded pixels. Therefore, it is straightforward to utilize PC-VI under a moving BSA configuration.

In the PC-VI based moving BSA method, the movement of the BSA is required more to fulfil the PC-VI requirement than for cumulative error reduction. Therefore, there is more flexibility in designing the BSA moving mode. In the following, two novel modes with better mechanical feasibility are proposed, i.e. twice interval scans with a static BSA and a lateral traversing BSA mode.

4.2.1. Twice interval scan with a static BSA. Scatter measurement by a static BSA is possible with the configuration described in section 3.3. It needs twice interval scan of half views, namely the first scan with a BSA for even views; and the second scan without BSA for odd views. On the one hand, scatter intensity in even views can be well measured in the first scan, and scatter fluence in odd views (second scan) can be well estimated from measurements of its neighbouring even views. On the other hand, the blocked primary fluence in the first scan can be restored by the complete odd views of the second scan, as seen in section 3.3.

4.2.2. Lateral traversing BSA mode. Lateral traversing is a simplified version of raster moving. It is a better choice since a 1D movement is easier to implement than the 2D movement. Under the lateral traversing mode, only certain slices suffer from artefacts due to blocking. However, this also makes this mode more demanding in terms of error reduction, since large cumulative errors tend to concentrate in certain slices.

Since the mode in section 4.2.1 has been evaluated in section 3.3, in the next section, the lateral traversing mode is evaluated with the raster-moving mode, under the setup of moving BSA measurement, where more influences (besides the quantum noise) are considered, such as scatter estimation residuals, polychromatic spectrum and the bowtie filter, and this is to investigate the reliability and practicability of the PC-VI based moving BSA method.

4.3. Evaluations

4.3.1. Simulation configuration. To generate scatter data, we simply revise the user code of normal transmission in EGSnrc (Kawrakow 2005): if photons were never scattered before they hit the detector, their weights are set to be zero. Thus the deposited energy on the detector is entirely due to the scattered photons. On this basis, to save the computational time, the RL fitting (Colijn and Beekman 2004a) is adopted to generate smooth scatter fluence with a small number of photons (N_{RL}). On the other hand, the primary fluence is computed by an analytical ray-tracing method (Tang *et al* 2008), with quantum noise added according to 10^6 photons per ray using a previously reported method (Patrick 2005). To match the proper SPR (scatter-to-primary ratio), i.e. the ratio of the RL-fitted scatter fluence (S_{RL}) to the primary fluence, MC simulations of the primary fluence (P_{MC}) with a large number of photons (N_{MC}) are performed in several sparse views. The SPR in view λ is estimated by

$$\text{SPR}(\lambda) = \frac{N_{\text{MC}} \sum_{u,v} S_{\text{RL}}(\lambda, u, v)}{N_{\text{RL}} \sum_{u,v} P_{\text{MC}}(\lambda, u, v)}. \quad (17)$$

To compute the SPR in other views, a cubic spline interpolation is adopted. Because the computed SPR is almost identical for all views, the same SPR is used in simulation. The spectrum is a 120 kVp GE rotating anode spectrum from the classical handbook of Thomas *et al* (1981). For a more detailed investigation of the spatial resolution, a $512 \times 512 \times 250$ humanoid phantom called *Visible Human* (Petoussi-Hens *et al* 2002, Zankl *et al* 2002) with a

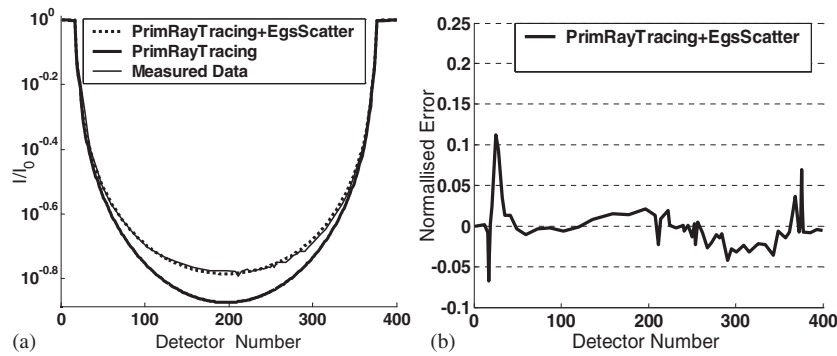


Figure 11. Validation of MC (EGSsrc) simulation. (a) Profiles of measured and simulated projections of the water phantom (logarithmic scale). (b) Normalized error of the simulated data corresponding to the same profile.

resolution of $0.91 \times 0.94 \times 5$ mm is used. The flat panel (*CsI*) has 1536×400 detectors with a resolution of 0.5 mm \times 0.5 mm. 1080 views are collected over 360° . A circular CBCT scan is simulated because it is more commonly used in practice. d_{soc} and d_{sod} (figure 10) are 750 mm and 1125 mm, respectively, to simulate the scatter-contaminated data. After that, d_{sob} is set to be 375 mm when simulating the measurements with a BSA, in which the key factor is the size of the BSA blocker. On one hand, the blocker should not be too large, since otherwise it will introduce extra frequency components and change the scatter distribution. On the other hand, it should not be too small, or else scatter measurement will be inaccurate. In our simulation, the blocker size is similar to that used in a previous experiment (Ning *et al* 2004), that is, 24×8 lead spheres with a diameter of 3 mm are embedded in the BSA, which blocks 12.5% of detectors; it is also similar to that used by Ning *et al* (2004) (10.8%). With this BSA, the lead sphere shadow in the detector periphery is about 10 mm \times 10 mm, in which the umbra shade is slightly larger than 1 mm \times 1 mm. Remember that the pixel size is 0.5 mm \times 0.5 mm; therefore, in the simulations with a BSA, the centred umbra scatter values of 2×2 pixels are averaged as the measurement, which is interpolated as the estimated scatter and subtracted from the scatter-contaminated data to get the scatter-removed data. In the scatter-removed data, 20×20 detectors are blinded at each position of the shadows since the shadow is about 10 mm \times 10 mm and the pixel size is 0.5 mm \times 0.5 mm, and the scatter-removed views with blocker shadows are acquired.

Evaluation of the agreement between the simulation and the experiment is made with the data from micro CT (Skyscan 1076). The parameters are from Colijn *et al* (2004b), where a homogenous water phantom is scanned. The result is shown in figure 11. Profiles of the simulated data match well with the experimental data: the average normalized error is below 5%. A relatively large error is observed near the edge due to a slight geometric misalignment between simulation and experiment.

4.3.2. Results. Comparisons of estimated and actual scatter components are performed in two typical views, as seen in figure 12. It shows that scatter estimation is quite accurate due to the high density of BSA sampling; the high-density design actually benefits from the power of PC-VI that can well restore the lost primary information.

One view of the *Visible Human* phantom (after the logarithm operation) is shown on the left of figures 13(a) and (b), for without and with a BSA, respectively. Three typical slices,

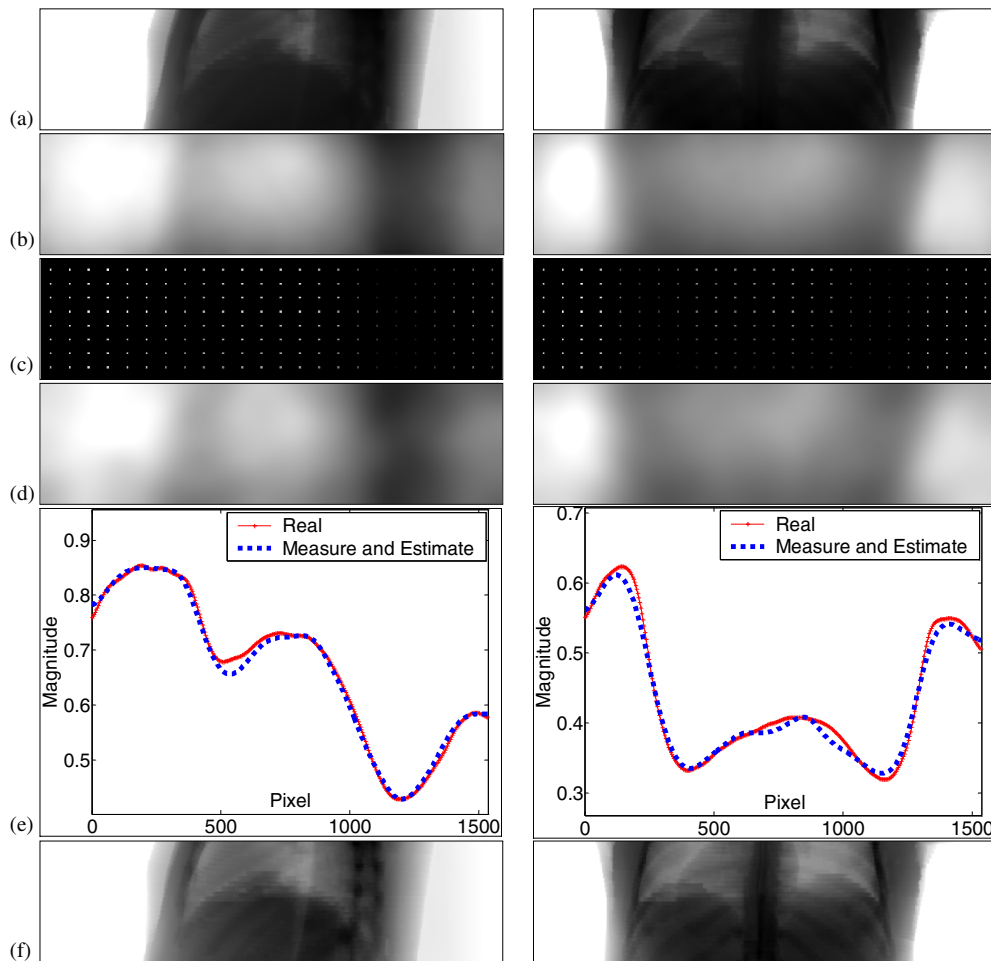


Figure 12. Typical views in the MC simulations. Left: side view, right: front view. For better contrast, the logarithmic scale is adopted in exhibiting (a), (c) and (e), with an adaptive adjustment of the window width [minimum, maximum] of the whole images. (a) The scatter-contaminated data. (b) The real scatter contained in (a). (c) The measurements with a BSA. (d) The estimated scatter from the measurements. (e) Comparison of the real and estimated scatter by the horizontal central profile. (f) Scatter removed data.

i.e. slice 2 (the centre slice), slice 1 (11.5 mm downward from slice 2) and slice 3 (10.5 mm upward from slice 2), are investigated under both raster-moving and lateral-traversing modes. The raster-moving trajectory is plotted on the right of figure 13(b). Images of size 1536×1536 are reconstructed by the FDK algorithm (Feldkamp *et al* 1984). The reconstructed images of the fan-beam scan and the scatter-contaminated CB scan are shown in figures 13(c)–(e).

Three referenced BSA based methods are compared. The first two methods are with a static BSA, namely I-BSA (Love *et al* 1987) and SV-BSA (Ning *et al* 2004). The third is the spatial interpolation based moving BSA method (Zhu *et al* 2004). In I-BSA implementation, scatter measurement is performed with a full-view extra scan with a BSA. In SV-BSA implementation, scatter intensity is measured every 20 views with a BSA, and hence the number of sparse views

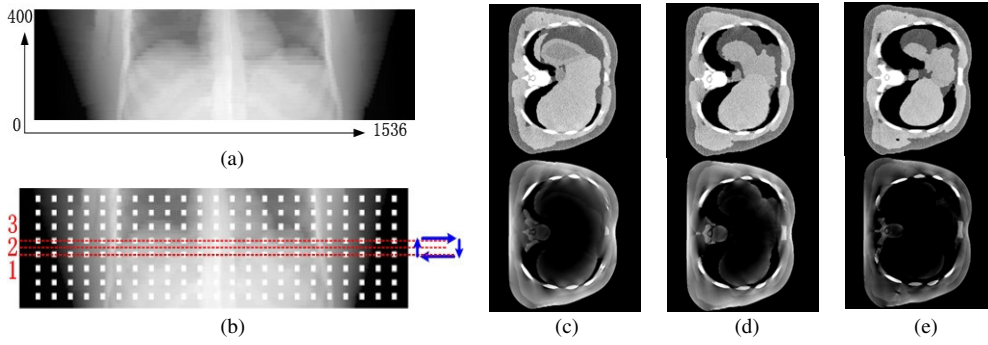


Figure 13. Left: one view of the *Visible Human*. (a) Without BSA. (b) With a BSA (raster-moving trajectory attached right). Right: reconstructed image with the fan-beam scan (top [−50, 200] HU) and scatter-contaminated CB scan (bottom [−300, 200] HU). (c)–(e) Slices 1–3.

is 54. The proportion of sparse views (i.e. 5% of the total views) is similar to the 4.88% reported by Ning *et al* (2004). The results are shown in figure 14.

In figure 14, rows 1, 3 and 5 show the reconstructed images of slices 1, 3 and 2 with the window [−50, 200] HU; rows 2, 4 and 6 show the difference images ([−50, 50] HU) relative to the fan-beam reconstruction, which is considered as the referenced scatter-free image. I-BSA, SV-BSA and the spatial interpolation based method as well as the PC-VI based method under two moving modes are shown from left to right. In SV-BSA, low-frequency fluctuations are observed in flat areas in all three slices. In the spatial interpolation based method, high-frequency streaks cause serious degradation of image quality. The streaks are eliminated to a large extent by PC-VI, and it can be seen that the results of the PC-VI based method appear to be visually similar to the I-BSA correction. When the raster-moving BSA moves in the lateral direction, slices 1 and 3 suffer a level of artefacts similar to the lateral mode. When it moves in the axial direction, slice 2 is blocked less seriously and suffers fewer artefacts. In the lateral mode, slice 2 is free of blocking and the reconstructed image is the same as the I-BSA correction; so those pictures are omitted.

The images in figure 14 are quantitatively investigated by using two classical indices. The results are listed in table 2. The first index is difference based, i.e. MSE (mean square error). RMSE (the relative value of the MSE) is defined in (18), where $\text{image}_{\text{Fan}}$ is the scatter-free image from the fan-beam scan. RMSE is ≥ 1 and lower RMSE means better similarity:

$$\text{RMSE} = \frac{\text{mean}(|\text{image}_{\text{Method}} - \text{image}_{\text{Fan}}|^2)}{\text{mean}(|\text{image}_{\text{I-BSA}} - \text{image}_{\text{Fan}}|^2)} \cdot 100\%. \quad (18)$$

The second index, namely MSSIM (multiscale structural similarity index) (Wang *et al* 2003), is a perception-based outstanding image quality assessment metric. The fan-beam image is used as the full reference as well. MSSIM is in the range of 0–1 and a larger MSSIM means better similarity.

To compare the spatial interpolation and PC-VI in the context of the moving BSA method, we define the reduced bias of RMSE as bias^- in (19). From table 2, we can calculate that bias^- in the range 6.27–16.52%, that is, the error of the spatial interpolation is reduced by about one order of magnitude (6.05–15.94) with PC-VI:

$$\text{bias}^- = \frac{\text{RMSE}_{\text{PC-VI}} - \text{RMSE}_{\text{I-BSA}}}{\text{RMSE}_{\text{SI}} - \text{RMSE}_{\text{I-BSA}}} \cdot 100\%. \quad (19)$$

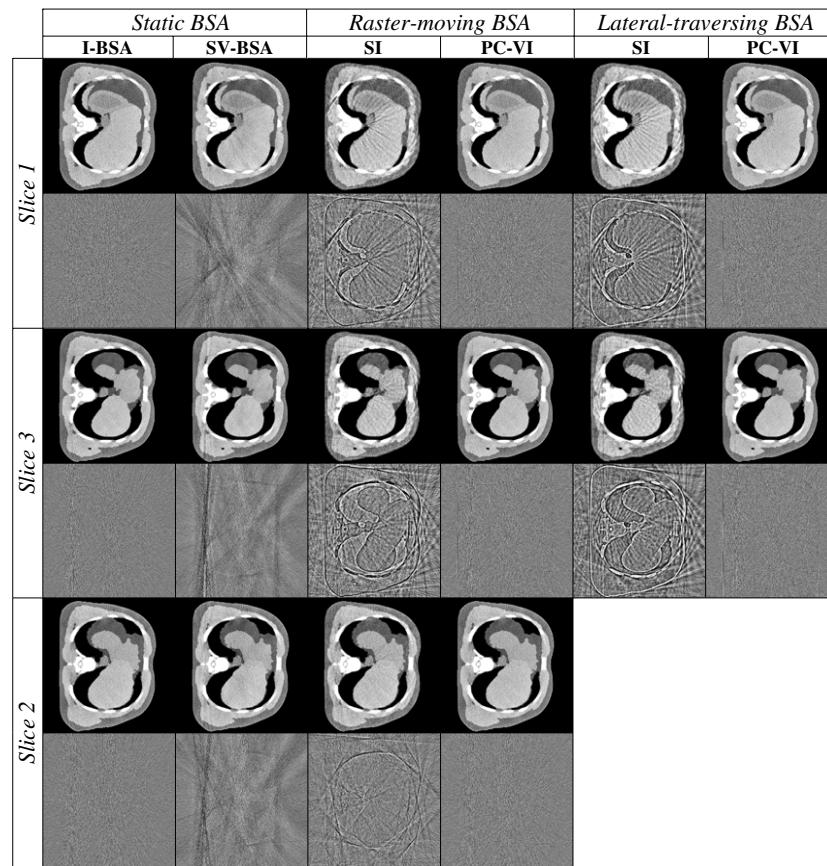


Figure 14. Results of three typical slices. The reconstructed images are shown in rows with odd numbers ($[-50, 200]$ HU) and the difference images are shown in rows with even numbers ($[-50, 50]$ HU). Left to right: I-BSA, SV-BSA, moving BSA method with SI and PC-VI under two moving modes. For the lateral mode, slice 2 is free of blocking and is the same as I-BSA.

Table 2. Comparison of different methods ('-' means the image is identical to that from I-BSA).

BSA mode	Method	RMSE			MSSIM		
		Slice 1	Slice 2	Slice 3	Slice 1	Slice 2	Slice 3
Static	I-BSA	1	1	1	0.9327	0.9385	0.9270
	SV-BSA	1.0213	1.0324	1.0708	0.9310	0.9369	0.9242
Raster	SI	1.2965	1.0875	1.4450	0.9047	0.9304	0.8814
	PC-VI (third cycle)	1.0207	1.0145	1.0735	0.9326	0.9381	0.9191
Lateral	SI	1.4324	-	1.5758	0.8971	-	0.8876
	PC-VI (third cycle)	1.0271	-	1.0931	0.9321	-	0.9233

Differences between the PC-VI based method and SV-BSA are generally small (table 2). Under the raster-moving mode, the PC-VI based method has advantages over SV-BSA in slices 1 2 with respect to both RMSE and MSSIM, but it is not as good as SV-BSA in slice 3.

Table 3. RMSE for horizontal slices crossing the centre of each shade under the lateral traversing mode.

Slice (row) number	39	85	131	177	223	269	315	361
Distance to the centre slice (mm)	-79.5	-55.5	-33.5	-10.5	11.5	34.5	57.5	80.5
SI	2.8260	2.6713	3.1565	3.6676	6.1690	9.1108	8.8197	9.1205
PC-VI (first cycle)	1.1168	1.1693	1.2198	1.2707	1.5634	2.0544	2.0244	1.7544
PC-VI (second cycle)	0.9961	1.0018	1.0193	1.0461	1.1506	1.2881	1.2776	1.2475
PC-VI (third cycle)	0.9824	0.9820	0.9914	1.0113	1.0858	1.1829	1.2035	1.2244

RMSE of I-BSA is normalized to 1.

Under the lateral-moving mode, PC-VI is better in slices 1 2 with respect to MSSIM, and in slice 2 with respect to RMSE also.

Furthermore, the PC-VI based method is evaluated comprehensively regarding every horizontal slice crossing the centres of the shades in figure 13(b). The slice number is counted by the row number, as shown in figure 13(a), and the distances of individual slices to the centre slice are also provided (table 3), where the negative sign means downward and positive upward. The corresponding values of RMSE are listed in table 3. The RMSE here is defined similar to (18) but is calculated in projections directly instead of the reconstructed images. Therefore, it is independent of the reconstruction method. From table 3, we see that PC-VI has an outstanding performance for each slice. For slices far below the lung cavity, i.e. slices 39, 85 and 131, the RMSE is less than 1(I-BSA), and this shows the potential of PC-VI in reducing noise caused by the use of the correlation between adjacent projections. A similar result in x-ray imaging was reported in Tischenko *et al* (2005) where the images acquired under slightly different imaging geometries were combined to reduce the anatomical noise. The improvement due to the PC-VI based method is more obvious for slices crossing the lung cavity, i.e. slices 269, 315 and 361, where several sharp edges between air and bone are present and much high-frequency information is lost. As illustrated in table 3, in these slices results have large values of RMSE (around 9) from spatial interpolation, which are decreased significantly to around 1.2 by PC-VI.

4.3.3. Preliminary study with a bowtie filter. On the necessity of incorporating a bowtie filter into CBCT, opinions vary greatly (Robert *et al* 2008, Mail *et al* 2009). Even so, investigation with a bowtie filter is necessary. Since the design of bowtie filters is challenging for CBCT, and there is no specified bowtie filter for CBCT (Mail *et al* 2009), only a preliminary study could be performed for this stage, using a z-axis invariant bowtie filter, which is also adopted to study the influence of the bowtie filter on CBCT imaging (Mail *et al* 2009). In this study, the bowtie filter is put 200 mm before the x-ray source; the lateral traversing mode is adopted; and the remaining parameters are the same as in section 4.3.2. The reconstructed images of slice 1 are shown in figure 15. Note that with a bowtie filter, using PC-VI, basically we still observe equivalent elimination of streaks, compared with figure 14.

5. Discussion

We propose a novel view interpolation method (PC-VI) based on the correlation between neighbouring CB projections. PC-VI reasonably utilizes redundant information in CB projections, as shown in figure 2. Therefore, it is reliable for restoring the primary fluence

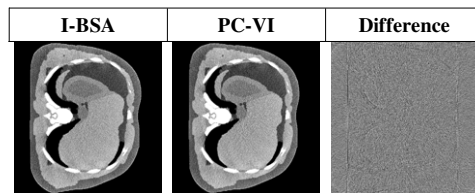


Figure 15. PC-VI (third cycle) performance with a bowtie filter. Reconstructed images are shown with the window $[-50, 200]$ HU and difference images are shown with the window $[-50, 50]$ HU.

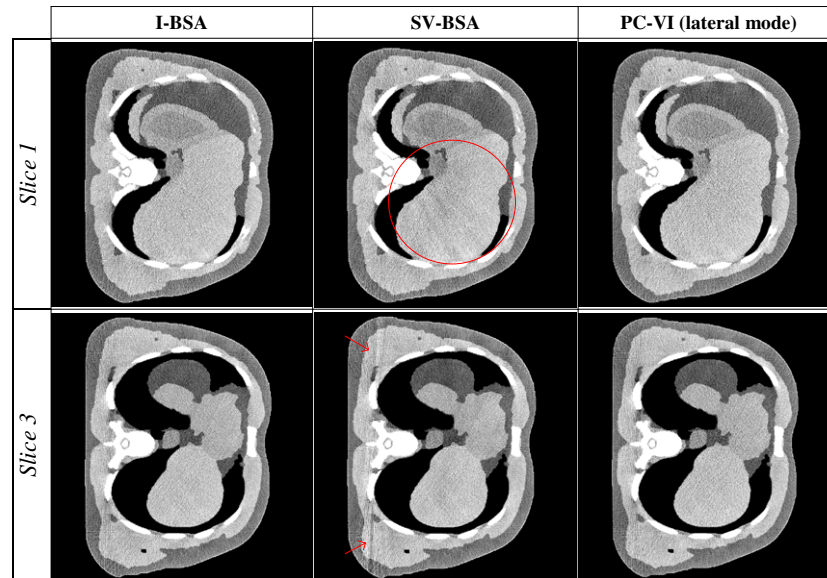


Figure 16. Further comparisons with enlarged images of slices 1–3. Displayed window: $[-50, 200]$ HU.

lost due to the BSA blocking, as seen in figures 4–6. PC-VI performs well with a normal number of views no less than 360 (figures 7, 8). The PC-VI requirement is easily satisfied in the moving BSA method (figure 9), and when it is satisfied, an arbitrary CB view could be well complemented with its neighbouring views by using PC-VI, as seen in figures 14 and 15.

The PC-VI based method is compared to the existing BSA based methods in section 4.3.2. It has great advantages over the spatial interpolation based method. Accordingly, the accuracy of the reconstructed images is improved by a factor of 6.05–15.94 (table 2). Further comparisons with SV-BSA show that the PC-VI based method has similar performance on the quality indices of RMSE and MSSIM; the observation that this method seems to have a better visual performance can be drawn from figure 16, where selected figures from figure 14 are enlarged. In each image of SV-BSA, there exist a few structural artefacts, i.e. the fluctuation in a flat area (inside the red circle) and the streak crossing the image (indicated by the red arrows). The underlying reason is that scatter estimation from sparse-view measurements is not accurate enough. On the other hand, only a slightly increased noise is observed in the images of the PC-VI based method, which are very similar to the images of I-BSA because

scatter intensities are well measured view by view, and the blocked primary fluence can be well restored by the proposed PC-VI.

When applied to a polychromatic spectrum with and without a bowtie filter, the reliability and practicability of the PC-VI based method are validated by the results shown in figures 14–15, although under these situations, PC is not strictly satisfied since it holds only for line integral. For the observation that even partial fulfilment of the PC is adequate for PC-VI to yield desirable results, the two probable reasons therein are (1) PC is at least quasi-fulfilled in this situation since it works only locally between two close rays which suffer similar levels of beam-hardening. (2) The polychromatic inconsistency is overruled by scatter artefacts that dominate under large cone angles. Recalling the argument that PC-VI works locally (section 3.4), the first reason (1) is supposed to be more relevant and it probably holds for other applications of John's equation as well. For example, the result with bowtie (figure 15) could be well understood by an analogy analysis: since the bowtie filter has nearly the same influences on two close rays, PC is also quasi-fulfilled; therefore PC-VI still works well when a bowtie filter is used.

Recall table 1, where the spatial interpolation based moving BSA method has *medium* accuracy in the primary fluence restoration. We think that the *medium* could be replaced by the *quasi-excellent* when we use the PC-VI based moving BSA method, which combines merits of dose efficiency, correction accuracy and mechanical feasibility. Concerning the mechanical feasibility, we would like to mention one more mode, rotating BSA, which is suggested because rotation usually has more mechanical reliability than translation; and artefacts from a rotating BSA are equally distributed in the whole reconstructed volume, and therefore, the primary fluence restoration might be much easier than for both lateral and raster modes.

PC-VI is a novel view interpolation method that angularly handles the redundant information in the frequency domain. Its potential applications include random malfunctioning pixel correction, truncation problem, metal artefact correction and few-view reconstruction. Whether this method would offer any concrete advantages in these potential applications and how effective it will be in these applications would mainly depend on the fulfilment level of the PC-VI requirement, and also on the amount of low-frequency information that can be initially restored by spatial interpolation.

6. Conclusion

A PC between neighbouring CB views is deduced. On this basis, the PC-VI is developed to fully utilize the CB redundant information. PC-VI works well under the condition that the angularly complementary information is known in either of the neighbouring views (PC-VI requirement).

The PC-VI based moving BSA method is proposed. It is far superior to the spatial interpolation based method. Its performance is similar to I-BSA. Considering this method also has efficient dose usage and flexible mechanical choice, it is supposed to be a candidate in the practical CBCT scatter correction methods.

Acknowledgments

This work is partially supported by National Natural Science Foundation of China (no 60551003), the fund of the Ministry of Education of China (no 20060698040) and the program of NCET of China (no NCET-05-0828). The authors would like to thank Dr Iwan Kawrakow for help using EGSnrc, and Dr Wojtek Zbijewski for help with coding of RL fitting and usage

of the measured data and Dr Lei Zhu and Dr Xiaobin Tang for help with phantom organ mapping. They also want to thank Dr Qin Chen for the revision and to the National high performance computing center (Xi'an, China) for MC computation.

References

- Boone J M 1988 An analytical model of the scattered radiation distribution in diagnostic radiology *Med. Phys.* **15** 721–25
- Cai W X, Ning R and Conover D 2008 Simplified method of scatter correction using a beam-stop-array algorithm for cone-beam computed tomography breast imaging *Opt. Eng.* **47** 097003
- Colijn A P and Beekman F J 2004a Accelerated simulation of cone-beam x-ray scatter projections *IEEE Trans. Med. Imaging* **23** 584–90
- Colijn A P, Zbijewski W, Sasov A and Beekman F J 2004b Experimental validation of a rapid Monte Carlo based micro-CT simulator *Phys. Med. Biol.* **49** 4321–33
- Defrise M, Noo F and Kudo H 2003 Improved two-dimensional rebinning of helical cone-beam computerized tomography data using John's equation *Inverse Problems* **19** S41–54
- Feldkamp L A, Davis L C and Kress J W 1984 Practical cone-beam algorithm *J. Opt. Soc. Am. A* **1** 612–9
- Floyd C E Jr, Chotas H and Ravin C E 1994 Scatter-reduction characteristics of an infinity-focused gridded radiographic cassette *Invest. Radiol.* **29** 852–55
- Graham S A, Moseley D J, Siewerdsen J H and Jaffray D A 2007 Compensator for dose and scatter management in cone-beam computed tomography *Med. Phys.* **34** 2691–03
- John F 1938 The ultrahyperbolic equation with 4 independent variables *Duke Math. J.* **4** 300–22
- Kawrakow I 2005 egsp: the EGSnrc C++ class library *NRCC Report PIRS-899*
- Kawrakow I and Rogers D 2003 The EGSnrc code system: simulation of electron and photon transport Ionizing radiation standards *Technical Report NRCC Rep. PIRS-701* (Ottawa: National Research Council of Canada)
- Kyriakou Y, Riedel T and Kalender W 2006 Combining deterministic and Monte Carlo calculations for fast estimation of scatter intensities in CT *Phys. Med. Biol.* **51** 4567–86
- Li H *et al* 2008 Scatter kernel estimation with an edge-spread function method for cone-beam computed tomography imaging *Phys. Med. Biol.* **53** 6729–48
- Love L A and Kruger R A 1987 Scatter estimation for a digital radiographic system using convolution filtering *Med. Phys.* **14** 178–85
- Mail N, Moseley D J, Siewerdsen J H and Jaffray D A 2009 The influence of bowtie filtration on cone-beam CT image quality *Med. Phys.* **36** 22–32
- Mainegra-Hing E and Kawrakow I 2008 Fast Monte Carlo calculation of scatter corrections for CBCT images *J. Phys. Conf. Ser.* **102** 012017
- Maltz J S, Blanz W E, Hristov D and Bani-Hashemi A R 2005 Cone beam X-ray scatter removal via image frequency modulation and filtering *27th Annu. Int. Conf. Eng. Med. Biol. Soc. (Shanghai)* pp 1854–57
- Maltz J S, Gangadharan B, Bose S, Hristov D H, Faddegon B A, Paidi A and Bani-Hashemi A R 2008a Algorithm for x-ray scatter, beam-hardening, and beam profile correction in diagnostic (kilovoltage) and treatment (megavoltage) cone beam CT *IEEE Trans. Med. Imaging* **27** 1791–80
- Maltz J S *et al* 2008b Focused beam-stop array for the measurement of scatter in megavoltage portal and cone beam CT imaging *Med. Phys.* **35** 2452–62
- Meyer M, Kalender W A and Kyriakou Y 2010 A fast and pragmatic approach for scatter correction in flat-detector CT using elliptic modeling and iterative optimization *Phys. Med. Biol.* **55** 99–120
- Ning R, Tang X and Conover D 2004 X-ray scatter correction algorithm for cone beam CT imaging *Med. Phys.* **31** 1195–202
- Patch S K 2002 Computation of unmeasured third-generation VCT views from measured views *IEEE Trans. Med. Imaging* **21** 801–13
- Patrick J L R 2005 Penalized-likelihood sinogram smoothing for low-dose CT *Med. Phys.* **32** 1676–83
- Persliden J and Carlsson G A 1997 Scatter rejection by air gaps in diagnostic radiology: calculations using a Monte Carlo collision density method and consideration of molecular interference in coherent scattering *Phys. Med. Biol.* **42** 155–75
- Petoussi-Hens N, Zankl M, Fill U and Regulla D 2002 The GSF family of voxel phantoms *Phys. Med. Biol.* **47** 89–106
- Poludniowski G, Evans P M, Hansen V N and Webb S 2009 An efficient Monte Carlo-based algorithm for scatter correction in keV cone-beam CT *Phys. Med. Biol.* **54** 3847–64
- Rinkel J *et al* 2007 A new method for x-ray scatter correction: first assessment on a cone-beam CT experimental setup *Phys. Med. Biol.* **52** 4633–52

- Robert C O, Michael J W and Michael D K 2008 C-arm cone-beam CT: general principles and technical considerations for use in interventional radiology *J. Vasc. Interv. Radiol.* **19** 814–21
- Schlattl H, Tischenko O and Hoeschen C 2006 Modeling of realistic raw data for image reconstruction—quantifying scattering noise in different CT geometries *Proc. SPIE* **6142** 614256
- Siewerdsen J H and Jaffray D A 2001 Cone-beam computed tomography with a flat-panel imager: magnitude and effects of x-ray scatter *Med. Phys.* **28** 220–31
- Siewerdsen J H, Moseley D J, Bakhtiar B, Moseley D J, Richard S, Keller H and Jaffray D A 2006 A simple, direct method for x-ray scatter estimation and correction in digital radiography and cone-beam CT *Med. Phys.* **33** 187–97
- Spies L, Evans P M, Partridge M, Hansen V N and Bortfeld T 2000 Direct measurement and analytical modeling of scatter in portal imaging *Med. Phys.* **27** 462–41
- Tang Shaojie *et al* 2008 Application of projection simulation based on physical imaging model to the evaluation of beam hardening corrections in x-ray transmission tomography *J. X-Ray Sci. Technol.* **16** 95–117
- Thomas R F, Ralph E S and Kermit R H Jr 1981 *Handbook of Computed Tomography X-Ray Spectra* (Rockville, MD: Bureau of Radiological Health) p 53
- Tischenko O, Hoeschen C and Buhr E 2005 Reduction of anatomical noise in medical x-ray images *Radiat. Prot. Dosim.* **114** 69–74
- Wang Z, Simoncelli E P and Bovik A C 2003 Multi-scale structural similarity for image quality assessment *IEEE Asilomar Conf. on Signals, Systems and Computers (Pacific Grove, CA)*
- Yan H, Mou X, Tang S and Xu Q 2009 Improved scatter correction in x-ray cone beam CT with moving beam stop array using John's equation *Proc. Int. Meeting on Fully Three-Dimensional Image Reconstruction in Radiology and Nuclear Medicine (Fully3D, Beijing, China)* pp 98–101
- Yao W and Leszczynski K 2009a An analytical approach to estimating the first order x-ray scatter in heterogeneous medium *Med. Phys.* **36** 3145–57
- Yao W and Leszczynski K 2009b An analytical approach to estimating the first order x-ray scatter in heterogeneous medium II. A practical application *Med. Phys.* **36** 3157–67
- Zankl M, Fill U, Petoussi-Hens N and Regulla D 2002 Organ dose conversion coefficients for external photon irradiation of male and female voxel models *Phys. Med. Biol.* **47** 2367–85
- Zbijewski W and Beekman F J 2006 Efficient Monte Carlo based scatter artefact reduction in cone-beam Micro-CT *IEEE Trans. Med. Imaging* **25** 817–27
- Zhu L, Bennett N R and Fahrig R 2006 Scatter correction method for x-ray CT using primary modulation: theory and preliminary results *IEEE Trans. Med. Imaging* **25** 1573–87
- Zhu L, Strobel N and Fahrig R 2004 X-ray scatter correction for cone beam CT using moving blocker array *Proc. SPIE* **5745** 251–8
- Zhu L, Xie Y, Wang J and Xing L 2009a Scatter correction for cone-beam CT in radiation therapy *Med. Phys.* **36** 2258–68
- Zhu L, Xie Y, Wang J and Xing L 2009b Noise suppression in scatter correction for cone-beam CT *Med. Phys.* **36** 741–52